


Article

# On Neural Observer in Dynamic Sliding Mode Control of Permanent Magnet Synchronous Wind Generator

Ali Karami-Mollaei<sup>1</sup> and Oscar Barambones<sup>2,\*</sup> 

<sup>1</sup> Faculty of Electrical and Computer Engineering, Hakim Sabzevari University, Sabzevar 9617976487, Iran; karami@hsu.ac.ir

<sup>2</sup> Automatic Control and System Engineering Department, University of the Basque Country, 01006 Vitoria-Gasteiz, Spain

\* Correspondence: oscar.barambones@ehu.eus

**Abstract:** The captured energy of a wind turbine (WT) can be converted into electricity by a generator. Therefore, to improve the efficiency of this system, both the structures of WTs and generators should be considered for control. But the present challenge is WT uncertainty, while the input signals to the generator should be smooth. In this paper, a permanent magnet synchronous generator (PMSG) is considered. The dynamics of the PMSG can be described using two axes, named d-q reference frameworks, with an input in each framework direction. To obtain the maximum power and to overcome the uncertainty by means of a smooth signal, the dynamic sliding mode controller (D-SMC) is implemented. In the D-SMC, an integrator is placed in the control scheme in order to suppress the chattering, because it acts like a low-pass filter. To estimate the state added by the integrator, a new observer-based neural network (ONN) is proposed. The proof of the stability of the D-SMC and ONN is based on Lyapunov theory. To prove the advantages of the D-SMC, a comparison was also carried out by traditional sliding mode control (T-SMC) with a similar ONN. From this comparison, we know that the advantages of the D-SMC are clear in terms of real implementation, concept, and chattering suppression.

**Keywords:** wind turbine; permanent magnet synchronous generator; observer-based neural network; sliding mode control; chattering

**MSC:** 93C10



**Citation:** Karami-Mollaei, A.; Barambones, O. On Neural Observer in Dynamic Sliding Mode Control of Permanent Magnet Synchronous Wind Generator. *Mathematics* **2024**, *12*, 2246. <https://doi.org/10.3390/math12142246>

Academic Editors: Mihail Ioan Abrudean, Vlad Muresan and António Lopes

Received: 17 June 2024  
Revised: 29 June 2024  
Accepted: 17 July 2024  
Published: 19 July 2024



**Copyright:** © 2024 by the authors. Licensee MDPI, Basel, Switzerland. This article is an open access article distributed under the terms and conditions of the Creative Commons Attribution (CC BY) license (<https://creativecommons.org/licenses/by/4.0/>).

## 1. Introduction

Global warming is a dangerous phenomenon posing a problem for the future of the Earth. It seems that using clean renewable energies such as wind and solar is the only approach for humans to reduce the effects of global warming [1,2], which are apparent in most countries [3]. However, due to the economical preference for and freely accessible nature of wind energy, many researchers are focusing on wind turbines (WTs) [4,5]. In past decades, fixed-speed WTs (FWTs) were used extensively [6,7], but in the case of wind speed change, FWTs have some limitations in capturing the maximum wind power [8]. Therefore, in recent years, variable-speed WTs (VWTs) have been constructed and used in industries [9]. The approach of maximum power capturing using VWTs is based on achieving the critical rated wind speed [10]. Below and above of this rate, the torque of the permanent magnet synchronous generator (PMSG) and pitch angle of the turbine blades (PATB) serve as the controller variables [11,12]. When the generator torque is controlled, the power coefficient is fixed. But when the power coefficient declines, the PATB is controlled to reduce the mechanical power of the captured wind so as not to exceed the nominal power of the VWT [11,12]. The other important wind speed boundaries which should be considered are cut-in and cut-out [11,12]. The WT would need to be shut down outside of this interval because of reasons linked to both economical and fatigue damage [13].

Therefore, torque control is an important issue in WTs [14–23], even in the presence of important challenges, i.e., drivetrain uncertainties, which can produce mechanical stress [8]. Hence, a robust controller should be designed to remove the effect of these uncertainties [15]. Many controllers have been proposed in the literature, though they are not robust, including the proportional–integral–derivative controller (PID) [16], the linear quadratic Gaussian controller (LQG) [17–19], the adaptive back-stepping controller [20], and model predictive control (MPC) [21]. Aside from them, the sliding mode controller (SMC) has the property of invariance and plays a powerful role in fighting against uncertainties [24,25]. The most prominent characteristic of the SMC is its invariance, since it is stronger than its robustness [26,27]. For this reason, many studies have focused on the torque control of WTs using the SMC [8,14,22,23,28,29]. Most of these methods have chattering as an unwanted phenomenon. For achieving the elimination of chattering, some methodologies have been presented [30], for example, the boundary layer SMC (B-SMC) [31,32], the adaptive boundary layer SMC (AB-SMC) [33,34], the higher-order SMC (H-SMC) [22,35,36], and the dynamic SMC (D-SMC) [26,27]. The most prominent property of the SMC, i.e., invariance, is missing in the B-SMC and AB-SMC [26–31]. Higher system model derivatives are needed in the H-SMC, which should be provided by observers [37–41]. In the D-SMC, a low-pass filter, such as an integrator, is set before the plant to remove the effect of chattering [26,27]. This increases the plant dimension. Therefore, in the D-SMC, the dynamics produced by this integrator should be estimated using a suitable observer [27]. However, in the H-SMC, an observer is needed to identify plant differentiation. This is the superior aspect of the D-SMC compared to the H-SMC.

The concepts of model identification [42,43], disturbance observer [28,29,44–46], and state observer [47,48] are used in a wide range of systems. Hence, these concepts refer to the estimation of unmeasurable or unknown parts of the systems or systems states. An observer is implemented by known system inputs and system outputs [42–51]. Based on the above discussion, using the D-SMC in WT torque control can help overcome both chattering and uncertainty to remove mechanical stress. Furthermore, to construct the D-SMC, a plant model is identified by an observer-based neural network (ONN). In this study, the stability of the ONN and D-SMC are proven by using Lyapunov approaches.

Therefore, based on the above discussion, chattering is a challenge in all of the mentioned works. Motivated by the above discussion about the drawbacks of other chattering suppression methods, we propose the use of the D-SMC in WT, connected to the PMSG for torque control. The proposed D-SMC was constructed by a new ONN to identify the plant model, preserve the invariance property and prevent chattering, and overcome mechanical stresses. A reliable comparison was carried out using the same ONN for both the D-SMC and T-SMC. Finally, to prove the stability of both the proposed controller and ONN, Lyapunov stability approaches are used.

Therefore, to put it concisely, the main contribution of this paper is its proposal of a new scheme for a D-SMC to control nonlinear WTs connected to a PMSG, which is modeled in d-q frameworks. The approach is chattering-free and based on a new observer-based neural network (ONN).

Six sections are presented to describe the construction of the proposed method. A complete model of a WT is demonstrated in Section 2. Then, the ONN and its proposed structure are described in Section 3. Section 4 is focused on a comparison and the proposed controller. Furthermore, the superiority of the proposed controller is shown by two simulations in Section 5. Finally, some conclusions are provided in Section 6.

## 2. Configuration and Structure of Turbine

The WT model consists of the generator part, the mechanical drivetrain part, and the aerodynamic part [22,52,53], which are shown in Figure 1, along with the model's corresponding signals.

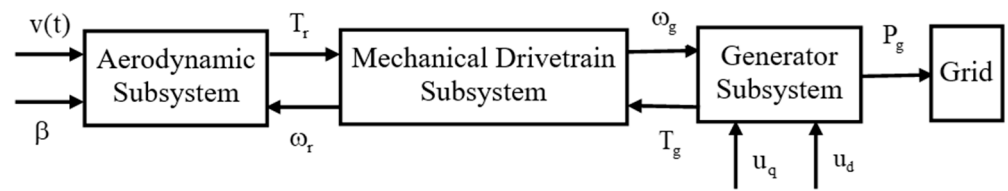


Figure 1. Subsystems and signals of the WT.

2.1. The Aerodynamic Part

The following equation describes the wind power generated by a WT, which is dependent on the blade length  $r$ , wind speed  $v(t)$ , air density  $\rho_a$ , and power coefficient  $C_p$  [14].

$$P_{wind} = \frac{\pi r^2 v^3 \rho_a}{2} C_p(\lambda, \beta) \tag{1}$$

Here,  $\lambda$  and  $\beta$  represent the tip speed ratio (TSR) and pitch blades, respectively. The TSR can be defined by dividing the tip blade’s linear velocity and wind speed [14].

$$\lambda = \frac{r\omega_r}{v} \tag{2}$$

In the above equation,  $\omega_r$  is the angular velocity of the rotor side. Based on Equation (1), the rotor torque or wind generated torque can be calculated as follows [14]:

$$T_r = \frac{P_{wind}}{\omega_r} = \frac{\pi r^3 v^2 \rho_a}{2\lambda} C_p(\lambda, \beta) \tag{3}$$

2.2. The Drivetrain Part

Although some papers have used a one-mass model [50], to have both a steady state and transient response [52], as well as a kinetic characteristic [53], in the WT, the mechanical drivetrain section should be modeled by a two-mass damper, as shown in Figure 2. This two-mass mechanical drivetrain is described by Equation (4), including the moment of inertia  $J_r$  and  $J_g$ , the external damping of  $K_r$  and  $K_g$ , and generator torque  $T_g$  [14].

$$\begin{aligned} J_r \dot{\omega}_r &= -K_r \omega_r + T_r - T_{ls} \\ J_g \dot{\omega}_g &= -K_g \omega_g - T_g + T_{hs} \end{aligned} \tag{4}$$

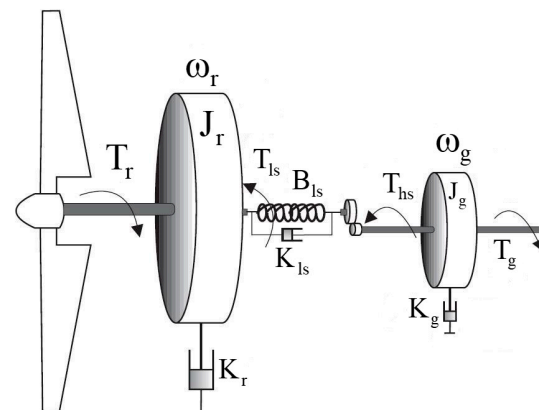


Figure 2. Mechanical model of WT.

As  $\omega_r$  is the angular velocity of the rotor side, the angular velocity of the generator side is  $\omega_g$ . The low-speed shaft braking torque  $T_{ls}$  is defined as follows [14]:

$$T_{ls} = K_{ls}(\omega_r - \omega_{ls}) + B_{ls}(\theta_r - \theta_{ls}) \tag{5}$$

Then, in the low-speed section, shaft angular speed, shaft angular velocity, shaft damping, and shaft stiffness are  $\theta_{ls}$ ,  $\omega_{ls}$ ,  $K_{ls}$ , and  $B_{ls}$ , respectively, and  $\theta_r$  is the speed deviation on the rotor side. Finally, the gearbox ratio, in an ideal case, can be defined as follows [14]:

$$n_g = \frac{T_{ls}}{T_{hs}} = \frac{\omega_g}{\omega_r} \tag{6}$$

Then, the second section of Equation (4) can be rewritten as

$$J_g(n_g\dot{\omega}_r) = -K_g(n_g\omega_r) - T_g + \left(\frac{T_{ls}}{n_g}\right) \tag{7}$$

or

$$n_g^2 J_g \dot{\omega}_r = -n_g^2 K_g \omega_r - n_g T_g + T_{ls} \tag{8}$$

In order to have all variables in the low-speed shaft, Equation (8) and the first section of Equation (4) should be combined:

$$J_t \dot{\omega}_r = -K_t \omega_r + T_r - n_g T_g \tag{9}$$

where  $J_t = J_r + n_g^2 J_g$ , and  $K_t = K_r + n_g^2 K_g$ .

### 2.3. The Permanent Magnet Synchronous Generator (PMSG) Part

A model of the PMSG, as two independent d-q dynamic current structures, can be described as follows [54,55]:

$$\begin{aligned} \dot{i}_q &= -\frac{R_g}{L_g} i_q - p\omega_g i_d - p\frac{\psi_f}{L_g} \omega_g + \frac{u_q}{L_g} \\ \dot{i}_d &= -\frac{R_g}{L_g} i_d + p\omega_g i_q + \frac{u_d}{L_g} \end{aligned} \tag{10}$$

where  $u_q$ ,  $i_q$ , and  $u_d$ ,  $i_d$  are the q-axis and d-axis voltage and current, respectively;  $R_g$  and  $L_g$  are stator resistance and inductance, respectively;  $\psi_f$  is the permanent magnet flux; and, finally,  $p$  is the number of pole pairs. Using Equation (6) yields the following results:

$$\begin{aligned} \dot{i}_q &= -\frac{R_g}{L_g} i_q - pn_g \omega_r i_d - p\frac{\psi_f}{L_g} n_g \omega_r + \frac{u_q}{L_g} \\ \dot{i}_d &= -\frac{R_g}{L_g} i_d + pn_g \omega_r i_q + \frac{u_d}{L_g} \end{aligned} \tag{11}$$

Moreover, the generator torque is  $T_g = \frac{3}{2}p\psi_f i_q + (L_d - L_q)i_d i_q$ , where  $L_d$  and  $L_q$  are the equivalent inductance in d-q directions. For a generator with flat poles, we have  $L_d = L_q$ , and therefore,  $T_g = \frac{3}{2}p\psi_f i_q$ .

### 3. The Observer-Based Neural Network (ONN) Proposed Approach

Based on the previous WT models, i.e., using the derivative of Equation (9) and the equation stating that  $\dot{T}_g = \frac{3}{2}p\psi_f \dot{i}_q$ , and then replacing the first part of Equation (11), the following equalities can be yielded:

$$\begin{aligned} \ddot{\omega}_r &= -\frac{K_t}{J_t} \dot{\omega}_r - n_g \frac{\dot{T}_g}{J_t} + \frac{\dot{T}_r}{J_t} = -\frac{K_t}{J_t} \dot{\omega}_r - n_g \frac{3p\psi_f \dot{i}_q}{2J_t} + \frac{\dot{T}_r}{J_t} \\ &= -\frac{K_t}{J_t} \dot{\omega}_r + \frac{3R_g pn_g \psi_f i_q}{2L_g J_t} + \frac{3p^2 n_g^2 \psi_f \omega_r i_d}{2J_t} + \frac{3p^2 n_g^2 \psi_f^2 \omega_r}{2L_g J_t} - \frac{3pn_g \psi_f u_q}{2L_g J_t} + \frac{\dot{T}_r}{J_t} \\ &= -\frac{K_t}{J_t} \dot{\omega}_r + \frac{R_g n_g}{L_g J_t} T_g + \frac{3p^2 n_g^2 \omega_r \psi_f i_d}{2J_t} + \frac{3p^2 n_g^2 \psi_f^2 \omega_r}{2L_g J_t} - \frac{3pn_g \psi_f u_q}{2L_g J_t} + \frac{\dot{T}_r}{J_t} \\ &= -\frac{K_t}{J_t} \dot{\omega}_r - \frac{R_g}{L_g} \dot{\omega}_r - \frac{R_g K_t}{L_g J_t} \omega_r + \frac{R_g T_r}{L_g J_t} + \frac{3p^2 n_g^2 \psi_f \omega_r i_d}{2J_t} + \frac{3p^2 n_g^2 \psi_f^2 \omega_r}{2L_g J_t} \\ &\quad - \frac{3pn_g \psi_f u_q}{2L_g J_t} + \frac{\dot{T}_r}{J_t} \\ &= \left(-\frac{K_t}{J_t} - \frac{R_g}{L_g}\right) \dot{\omega}_r + \left(\frac{3p^2 n_g^2 \psi_f i_d}{2J_t} + \frac{3p^2 n_g^2 \psi_f^2}{2L_g J_t} - \frac{R_g K_t}{L_g J_t}\right) \omega_r - \frac{3pn_g \psi_f}{2L_g J_t} u_q \\ &\quad + \frac{R_g T_r}{L_g J_t} + \frac{\dot{T}_r}{J_t} \end{aligned} \tag{12}$$

Note that the last equation is obtained after rearranging. For power factor correction or compensation (PFC), the current of the d – axis is set to zero, i.e.,  $i_d = 0$ , and therefore, from Equation (11), we have  $u_d = -L_g p n_g \omega_r i_q$ . Hence,

$$\ddot{\omega}_r = \left(-\frac{K_t}{J_t} - \frac{R_g}{L_g}\right)\dot{\omega}_r + \left(\frac{3p^2 n_g^2 \psi_f^2}{2L_g J_t} - \frac{R_g K_t}{L_g J_t}\right)\omega_r - \left(\frac{3p n_g \psi_f}{2L_g J_t}\right)u_q + \left(\frac{R_g T_r}{L_g J_t} + \frac{\dot{T}_r}{J_t}\right) \tag{13}$$

For simplicity, the state variables  $x_1 = \omega_r$  and  $x_2 = \dot{\omega}_r$ , with the following linear state feedback, are defined:

$$u_q = \frac{2L_g J_t}{3p n_g \psi_f} \left[ \left(-\frac{K_t}{J_t} - \frac{R_g}{L_g} + a_2\right)x_2 + \left(\frac{3p^2 n_g^2 \psi_f^2}{2L_g J_t} - \frac{R_g K_t}{L_g J_t} + a_1\right)x_1 - z(t) \right] \tag{14}$$

where  $z$  is the new input control signal; now, Equation (13) can be rewritten as follows:

$$\dot{x} = Ax + Bz + B\Delta \tag{15}$$

where  $\Delta$  is an unknown part, and

$$A = \begin{bmatrix} 0 & 1 \\ -a_1 & -a_2 \end{bmatrix}, B = \begin{bmatrix} 0 \\ 1 \end{bmatrix}, x = \begin{bmatrix} x_1 \\ x_2 \end{bmatrix} \tag{16}$$

$$\Delta = \frac{R_g T_r}{L_g J_t} + \frac{\dot{T}_r}{J_t} \tag{17}$$

In the above equation,  $a_1$  and  $a_2$  are constants and are selected in order to have a Hurwitz matrix  $A$ . Matrix  $A$  is a Hurwitz matrix if, for any matrix  $Q$  (symmetric positive definite), a matrix  $P$  (symmetric positive definite) can be find from the following Lyapunov equation:

$$A^T P + PA = -Q \tag{18}$$

Using the D-SMC for system Equation (15), the sliding surface is defined as follows:

$$s = c_1(\omega_r - \omega_{rd}) + c_2(\dot{\omega}_r - \dot{\omega}_{rd}) + c_3(\ddot{\omega}_r - \ddot{\omega}_{rd}) = c_1(x_1 - \omega_{rd}) + c_2(x_2 - \dot{\omega}_{rd}) + c_3(\dot{x}_2 - \ddot{\omega}_{rd}) \tag{19}$$

However, variable  $\dot{x}_2$  is not accessible due to the unknown variable  $\Delta$ . This variable is unknown and can be considered as the uncertainty because  $T_r$  and  $\dot{T}_r$  are completely unknown. These variables are unknown because various power factors,  $C_p$ , are used in the literature [45,53]. To calculate this variable, a new ONN structure is proposed, as described in the following paragraphs.

Since neural networks have the property of universal approximation [26], one can find some weights  $\Theta$  for the continuous function  $\Delta$  so that

$$\Delta = \Theta^T \Phi(x) + \varepsilon(x) \tag{20}$$

where the neural network approximation error is norm-bounded, i.e.,  $\|\varepsilon(x)\| \leq F_\varepsilon$ , and  $\Theta \in R^{2 \times 1}$  is the unknown weight vector; also,  $\Phi(x) = [\phi_1(x), \phi_2(x)]^T$  is the Sigmoidal function in the hidden layer.

$$\begin{aligned} \phi_i(x) &= \frac{2}{1 + \exp(-2N_i x)} - 1 : i = 1, 2 \\ N_i &= [n_1, n_2] \\ n_j &= \begin{cases} 0 & : j \neq i \\ 1 & : j = i \end{cases} \end{aligned} \tag{21}$$

Hence, Equation (15) can be expressed as follows:

$$\dot{x} = Ax + Bz + B(\Theta^T \Phi + \varepsilon) \tag{22}$$

Nevertheless, Equation (22) is described by the following approximate model:

$$\dot{\hat{x}} = A\hat{x} + Bz + B\hat{\Theta}^T \Phi(x) \tag{23}$$

The identification error can be defined as follows:

$$\begin{aligned} \tilde{x} &= x - \hat{x} \\ \tilde{\Theta} &= \Theta - \hat{\Theta} \end{aligned} \tag{24}$$

From Equations (22) and (23) and their subtraction, one can conclude that

$$\dot{\tilde{x}} = A\tilde{x} + B(\tilde{\Theta}^T \Phi(x) + \varepsilon) \tag{25}$$

**Theorem 1.** *When the adaptive weight is updated based on the following equation, the error  $\tilde{x} = x - \hat{x}$  converges to zero.*

$$\dot{\hat{\Theta}} = \rho_1 A \Phi \|\tilde{x}\| - \rho_2 \hat{\Theta} \|\tilde{x}\| \tag{26}$$

The above includes the use of scalars  $\rho_1 > 0$  and  $\rho_2 > 0$ , which are constant.

**Proof.** We proceed with the Lyapunov function as the sum of two quadratic sections.

$$V = \frac{1}{2} \tilde{x}^T P \tilde{x} + \frac{1}{2\rho_2} \tilde{\Theta}^T \tilde{\Theta} \tag{27}$$

Derivative of Lyapunov Equation (27) with respect to time leads to the following:

$$\dot{V} = \frac{1}{2} \tilde{x}^T P \dot{\tilde{x}} + \frac{1}{2} \dot{\tilde{x}}^T P \tilde{x} + \frac{1}{\rho_2} \tilde{\Theta}^T \dot{\tilde{\Theta}} \tag{28}$$

In the above,  $\dot{\tilde{\Theta}} = -\dot{\hat{\Theta}}$ ; now, using Equations (18), (25), and (26) in Equation (28) results in the following:

$$\dot{V} = \tilde{x}^T P B (\Theta^T \Phi + \varepsilon) - \frac{1}{2} \dot{\tilde{x}}^T Q \tilde{x} + \frac{\rho_1}{\rho_2} \tilde{\Theta}^T A \Phi \|\tilde{x}\| + \tilde{\Theta}^T \tilde{\Theta} \|\tilde{x}\| \tag{29}$$

Consider the following inequality [24]:

$$-\tilde{x}^T Q \tilde{x} \leq -\lambda_{\min}(Q) \|\tilde{x}\|^2 < 0 \tag{30}$$

And consider that

$$\begin{aligned} \tilde{\Theta}^T \dot{\hat{\Theta}} &= \tilde{\Theta}^T (\Theta - \tilde{\Theta}) \leq F_{\Theta} \|\tilde{\Theta}\| - \|\tilde{\Theta}\|^2 \\ \tilde{\Theta}^T A \Phi &\leq F_{\Phi} \|\tilde{\Theta}\| \|A\| \end{aligned} \tag{31}$$

where  $\lambda_{\min}$  denotes the minimum eigen-value, and  $F_{\Phi}$  and  $F_{\Theta}$  are the bounds of neural network parameters.

$$\|\Theta^T\| = \|\Theta\| \leq F_{\Theta}, \|\Phi^T\| = \|\Phi\| \leq F_{\Phi} \tag{32}$$

Therefore,

$$\begin{aligned} \dot{V} &\leq -\frac{1}{2} \lambda_{\min}(Q) \|\tilde{x}\|^2 + \|\tilde{x}\| \|P\| \|B\| \left( \|\tilde{\Theta}\| F_{\Phi} + F_{\varepsilon} \right) \\ &\quad + \frac{\rho_1}{\rho_2} F_{\Phi} \|\tilde{\Theta}\| \|A\| \|\tilde{x}\| + \left( F_{\Theta} \|\tilde{\Theta}\| + \|\tilde{\Theta}\|^2 \right) \|\tilde{x}\| \end{aligned} \tag{33}$$

Taking into account  $\|B\| = 1$  results in the following:

$$\dot{V} \leq -\frac{1}{2}\lambda_{\min}(Q)\|\tilde{x}\|^2 + \left( \|P\|F_\varepsilon - \left[ \|\tilde{\Theta}\|^2 - \left( \|P\|F_\Phi + F_\Theta + \frac{\rho_1}{\rho_2}F_\Phi\|A\| \right) \|\tilde{\Theta}\| \right] \right) \|\tilde{x}\| \tag{34}$$

Now, we define  $F_{\tilde{x}}$ :

$$F_{\tilde{x}} = \frac{\|P\|F_\varepsilon - \frac{1}{4}\left( \|P\|F_\Phi + F_\Theta + \frac{\rho_1}{\rho_2}F_\Phi\|A\| \right)^2}{\frac{1}{2}\lambda_{\min}(Q)} \tag{35}$$

Then,

$$\dot{V} \leq -\frac{1}{2}\lambda_{\min}(Q)(\|\tilde{x}\| - F_{\tilde{x}}) \|\tilde{x}\| - \left( \|\tilde{\Theta}\| - \frac{1}{2}\left[ \|P\|F_\Phi + F_\Theta + \frac{\rho_1}{\rho_2}F_\Phi\|A\| \right] \right)^2 \|\tilde{x}\| \tag{36}$$

or

$$\dot{V} \leq -\frac{1}{2}\lambda_{\min}(Q)(\|\tilde{x}\| - F_{\tilde{x}}) \|\tilde{x}\| \tag{37}$$

Suppose  $\|\tilde{x}\| > F_{\tilde{x}}$ ; therefore,  $\dot{V} \leq -0.5\lambda_{\min}(Q)(\|\tilde{x}\| - F_{\tilde{x}}) \|\tilde{x}\| \leq 0$ , which leads to the following:

$$\begin{aligned} 0 &\leq \int_0^t 0.5(\|\tilde{x}(\tau)\| - F_{\tilde{x}}) \|\tilde{x}(\tau)\| \lambda_{\min}(Q) d\tau \\ &\leq \int_0^t 0.5(\|\tilde{x}(\tau)\| - F_{\tilde{x}}) \|\tilde{x}(\tau)\| \lambda_{\min}(Q) d\tau + V(t) \leq V(0) \end{aligned} \tag{38}$$

This inequality is true even if  $t \rightarrow \infty$ , since  $V(0)$  is finite and positive. Therefore, the Barbalat’s lemma [24] results in the following:

$$\lim_{t \rightarrow \infty} 0.5(\|\tilde{x}\| - F_{\tilde{x}}) \|\tilde{x}\| \lambda_{\min}(Q) = 0 \tag{39}$$

It is clear that  $\lambda_{\min}(Q)$  is greater than zero, so Equation (39) causes a decrease in  $\|\tilde{x}\|$  into the bound of  $F_{\tilde{x}}$ , i.e.,  $\lim_{t \rightarrow \infty} \|\tilde{x}\| \leq F_{\tilde{x}}$ .  $\square$

**Remark 1.** Parameters  $\rho_1$  and  $\rho_2$  are selected in order to prevent drift in Equation (26).

#### 4. Sliding Mode Controller (SMC) Design

In this section, two new approaches are proposed: the D-SMC and T-SMC. In both of them, the same presented ONN of Equation (23) is used to ensure a trustworthy comparison.

##### 4.1. The Proposed D-SMC Approach

As has been mentioned, variable  $\dot{x}_2$  is not accessible in Equation (39). To this end, the ONN in Equation (23) is proposed. Substituting the observer equation (Equation (23)) and Equation (26) into the sliding surface equation (Equation (19)) results in the following:

$$s = c_1(\hat{x}_1 - \omega_{rd}) + c_2(\hat{x}_2 - \dot{\omega}_{rd}) + c_3(\dot{\hat{x}}_2 - \ddot{\omega}_{rd}) \tag{40}$$

Hence, by definition of  $G = [0, 1]$ , we have the following (note that  $GB = 1$ ):

$$\begin{aligned} \dot{s} &= c_1(\dot{\hat{x}}_2 - \dot{\omega}_{rd}) + c_2(GA\hat{x} + z + \hat{\Theta}^T\Phi - \ddot{\omega}_{rd}) \\ &+ c_3\left( GA\left[ A\hat{x} + Bz + B\hat{\Theta}^T\Phi \right] + \dot{z} + \left[ \rho_1A\Phi\|\tilde{x}\| - \rho_2\hat{\Theta}\|\tilde{x}\| \right]^T\Phi + \hat{\Theta}^T\Phi - \ddot{\omega}_{rd} \right) \end{aligned} \tag{41}$$

or

$$\begin{aligned} \dot{s} &= c_1(\dot{\hat{x}}_2 - \dot{\omega}_{rd}) + c_2(GA\hat{x} + z + \hat{\Theta}^T\Phi - \ddot{\omega}_{rd}) \\ &+ c_3\left( GA^2\hat{x} + GABz + GAB\hat{\Theta}^T\Phi + \dot{z} + \rho_1\Phi^TA^T\|\tilde{x}\|\Phi - \rho_2\hat{\Theta}^T\|\tilde{x}\|\Phi + \hat{\Theta}^T\Phi - \ddot{\omega}_{rd} \right) \end{aligned} \tag{42}$$

**Theorem 2.** The reaching-to-sliding surface equation (Equation (19)) is provided in finite time if the following chattering-free signal is used as the input control for the system (Equation (15)).

$$\dot{z} = \frac{-c_1(\hat{x}_2 - \dot{\omega}_{rd}) + c_2(GA\hat{x} + z + \hat{\Theta}^T\Phi - \dot{\omega}_{rd}) - \frac{c_3(GA^2\hat{x} + GABz + GAB\hat{\Theta}^T\Phi + \dot{z} + \rho_1\Phi^T A^T \|\hat{x}\|\Phi - \rho_2\hat{\Theta}^T \|\hat{x}\|\Phi + \hat{\Theta}^T\Phi - \ddot{\omega}_{rd})}{c_3} - \frac{h_1 \text{sign}(s) + h_2 s}{c_3}}{c_3} \quad (43)$$

The above includes the constant parameters  $h_1$  and  $h_2$ .

**Proof.** Considering Equations (42) and (43) provides the following:

$$\dot{s} = -h_1 \text{sign}(s) - h_2 s \quad (44)$$

Using  $V = 0.5s^2$  as the Lyapunov function leads to the following:

$$\dot{V} = s\dot{s} = s(-h_1 \text{sign}(s) - h_2 s) = -h_1 |s| - h_2 s^2 \leq -h_1 |s| \quad (45)$$

Consider  $t_f$  and suppose that  $s(t_f) = 0$ ; then, it can be shown that  $t_f \leq \frac{|s(0)|}{h_1}$  [24].  $\square$

**Remark 2.** Parameter  $h_1$  is selected to enable reaching to the sliding surface in a small time  $t_f$  and parameter  $h_2$  is selected to ensure good performance for the closed loop system.

Note that the implemented proposed D-SMC and ONN are presented in Figure 3.

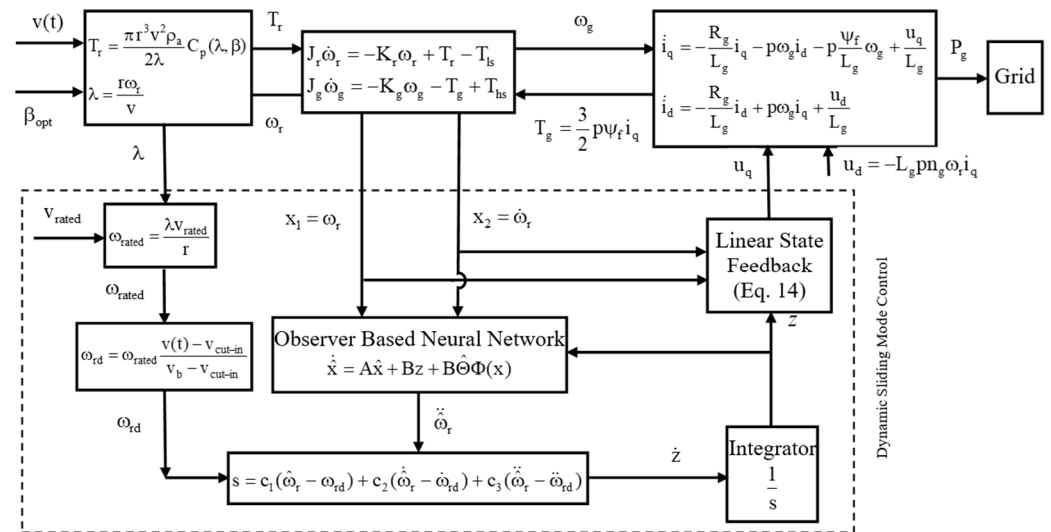


**Figure 3.** The proposed configuration diagram.

As explained before and shown in this figure, the sliding surface  $s$  is calculated based on the reference of rotor angular velocity  $\omega_{rd}$ , as well as the neural observer output  $\hat{\omega}_r$ . Then,  $\dot{z}$  is calculated and  $z$  obtained via the integration of  $\dot{z}$ . Finally,  $u_q$  is obtained using state feedback.

#### 4.2. The Proposed T-SMC Approach

Consider the following sliding surface:

$$s = c_1(\hat{x}_1 - \omega_{rd}) + c_2(\hat{x}_2 - \dot{\omega}_{rd}) \quad (46)$$



Using Equation (23) and equality  $GB = 1$  results in the following:

$$\dot{s} = c_1(\hat{x}_2 - \dot{\omega}_{rd}) + c_2(GA\hat{x} + z + \hat{\Theta}^T\Phi - \dot{\omega}_{rd}) \tag{47}$$

**Theorem 3.** *The reaching-to-sliding surface equation (Equation (46)) is carried out in finite time if the following signal is used as the input control for the system equation (Equation (15)).*

$$z = -\frac{c_1(\hat{x}_2 - \dot{\omega}_{rd}) + c_2(GA\hat{x} + \hat{\Theta}^T\Phi - \ddot{\omega}_{rd}) + h_1\text{sign}(s) + h_2s}{c_2} \tag{48}$$

The above includes the constant parameters  $h_1$  and  $h_2$ .

**Proof.** Substituting Equation (48) into Equation (47), we can conclude that:

$$\dot{s} = -h_1\text{sign}(s) - h_2s \tag{49}$$

Then, the Lyapunov function,  $V = 0.5s^2$ , results in the following:

$$\dot{V} = s\dot{s} = s(-h_1\text{sign}(s) - h_2s) = -h_1|s| - h_2s^2 \leq -h_1|s| \tag{50}$$

Consider  $t_f$  and suppose that  $s(t_f) = 0$ ; then, it can be shown that  $t_f \leq \frac{|s(0)|}{h_1}$  [24]. Hence, proof is obtained.  $\square$

### 4.3. The Reference of Rotor Angular Velocity

Based on Figure 4, the VWT operation mode is divided by a known rated index into four regions. When the wind speed is smaller than cut-in, VWT is shut down because of the economic conditions. The pitch blades of a VWT are set to its constant optimal value, and generator torque is controlled for the wind speed bigger than the cut-in wind speed and smaller than the rated wind speed. For this operation mode, the maximum power coefficient is provided by increasing rotor speed. For the wind speed bigger than the rated wind speed and smaller than the cut-out wind speed, the pitch angle of the blades is increased to reduce the rotor speed. In this case, the generator power is regulated to its rated value. Finally, for protection against fatigue damage, the VWT is shut down above the cut-out operation mode [13].

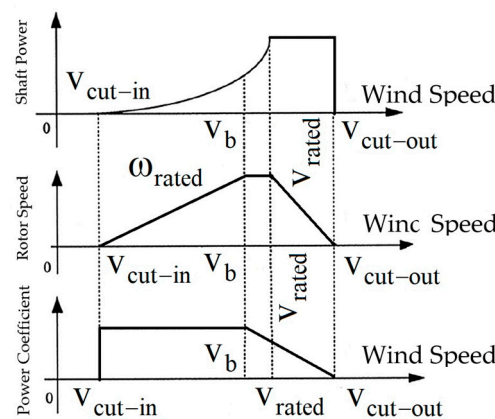


**Figure 4.** Operation regions of VWT.

From Figure 4, in the second operation mode and for torque control, the reference of rotor angular velocity can be written as follows:

$$\omega_{rd} = \omega_{rated} \frac{v(t) - v_{cut-in}}{v_b - v_{cut-in}} \quad (51)$$

According to Equation (2), it is clear that:

$$\omega_{rated} = \frac{\lambda v_{rated}}{r} \quad (52)$$

We use a two-mass VWT with a power of 5 MW which is placed in the National Renewable Energy Laboratory (NREL) in Colorado. The parameters of this WT are presented in Table 1 [56].

**Table 1.** VWT parameters.

Parameter	Value	Unit
$v_{cut-in}$	3	m/s
$v_b$	10.2	m/s
$v_{rated}$	11.4	m/s
$v_{cut-out}$	25	m/s
$\beta_{opt}$	0	deg
$\lambda_{opt}$	7.55	rad

In addition, due to the use of the NREL WT, the parameters of the mechanical part are also listed in Table 2 [56].

**Table 2.** VWT drivetrain parameters.

Notation	Value	Unit
$r$	21.62	m
$\rho_a$	1.308	kg/m <sup>3</sup>
$J_r$	$3.25 \times 10^5$	kg × m <sup>2</sup>
$J_g$	34.4	kg × m <sup>2</sup>
$K_r$	27.36	(N × m)/(rad/s)
$K_g$	0.2	(N × m)/(rad/s)
$K_{ls}$	$9.5 \times 10^3$	(N × m)/rad
$B_{ls}$	$2.691 \times 10^5$	(N × m)/(rad/s)
$n_g$	43.165	Scalar

Furthermore, the parameters of the PMSG are specified in Table 3.

**Table 3.** The PMSG parameters.

Notation	Value	Unit
$R_g$	2	Ohm
$L_g$	12	Henry
$\psi_f$	25	Weber
$p$	12	Scalar

### 5. Simulation Results

Both the D-SMC and T-SMC were simulated using the parameters of  $a_1 = 1$  and  $a_2 = 2$  for the state feedback. Moreover, the same proposed ONN was used in both approaches for a reliable comparison. Moreover, the initial values of ONN weights were set to zero, i.e.,  $\Theta_1(0) = \Theta_2(0) = 0$ . Also, we chose  $h_1 = 5$ ,  $h_2 = 20$ ,  $\rho_1 = 1$ , and  $\rho_2 = 5$ . The wind speed and the reference of rotor speed, denoted by Equation (51), are shown in Figures 5 and 6, respectively. Note that this wind speed is in the second region, with a mean value of 7 and added white noise to simulate a read wind.

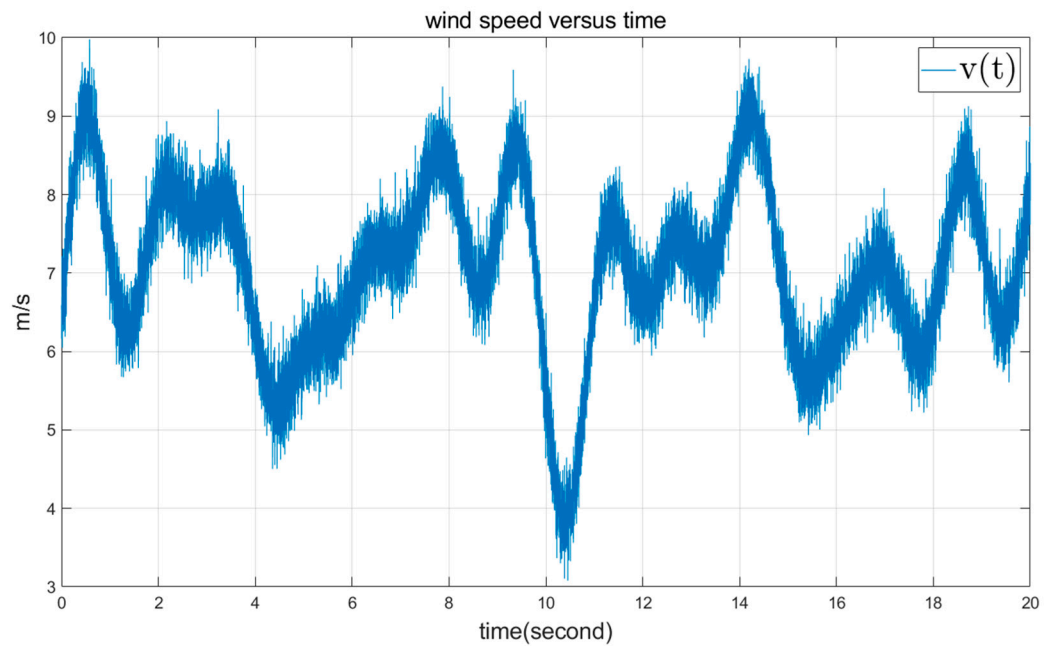


Figure 5. Time series of wind profile.

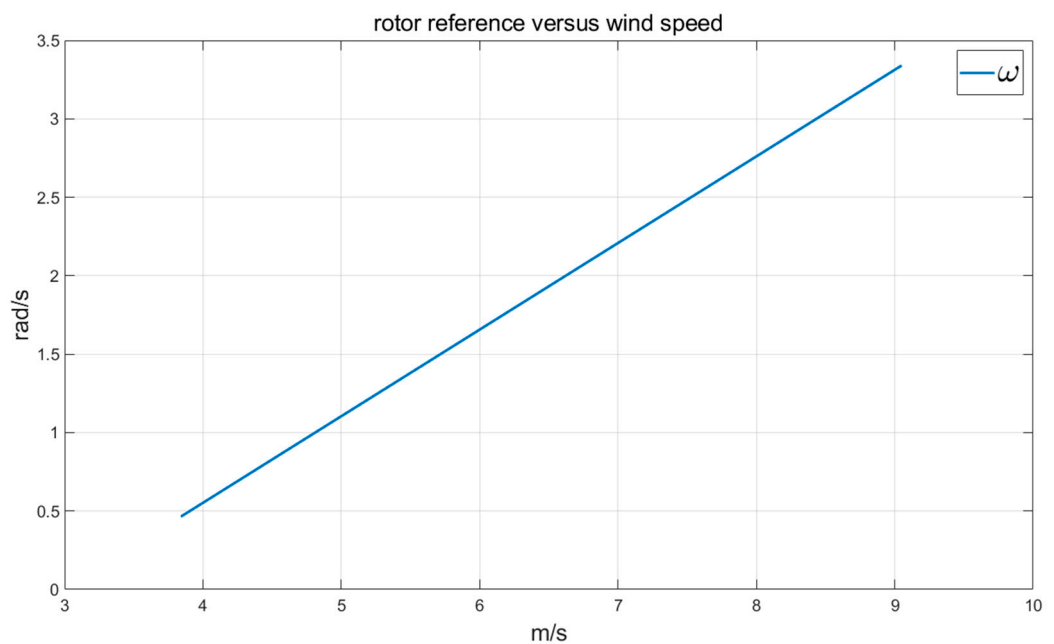


Figure 6. Angular velocity of rotor reference.

In the proposed D-SMC approach, the sliding surface coefficients are selected as  $c_1 = 10$ ,  $c_2 = 0.1$ , and  $c_3 = 0.01$ . This selection causes the zero dynamics of sliding surface

(19) or (40) to be set to zero, i.e., when the sliding surface reaches zero in finite time, the sliding variables converge to zero. The initial value of  $z(0)$  is set to zero, i.e.,  $z(0) = 0$ . This is needed for the calculation of the input control signal from Equation (43). Figures 7–10 show the simulation results. Figure 7 shows the sliding surface, which converges to zero in finite time. Figure 8 shows the performance of the proposed ONN. Reference signal tracking can also be seen from this figure. In Figure 9, the torque input control signal of the PMSG in the q-axis is depicted. This chattering-free signal is also the D-SMC output. The adaptive weights of the ONN are shown in Figure 10. Note that the initial oscillations in Figures 9 and 10 are not chattering.

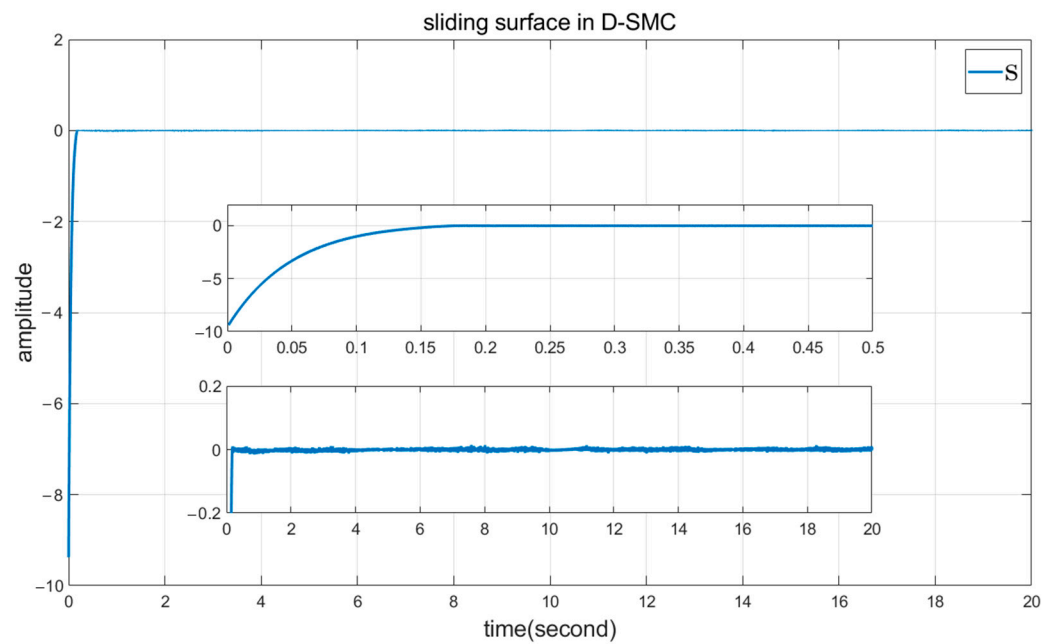


Figure 7. Finite-time sliding surface convergence to zero using D-SMC.

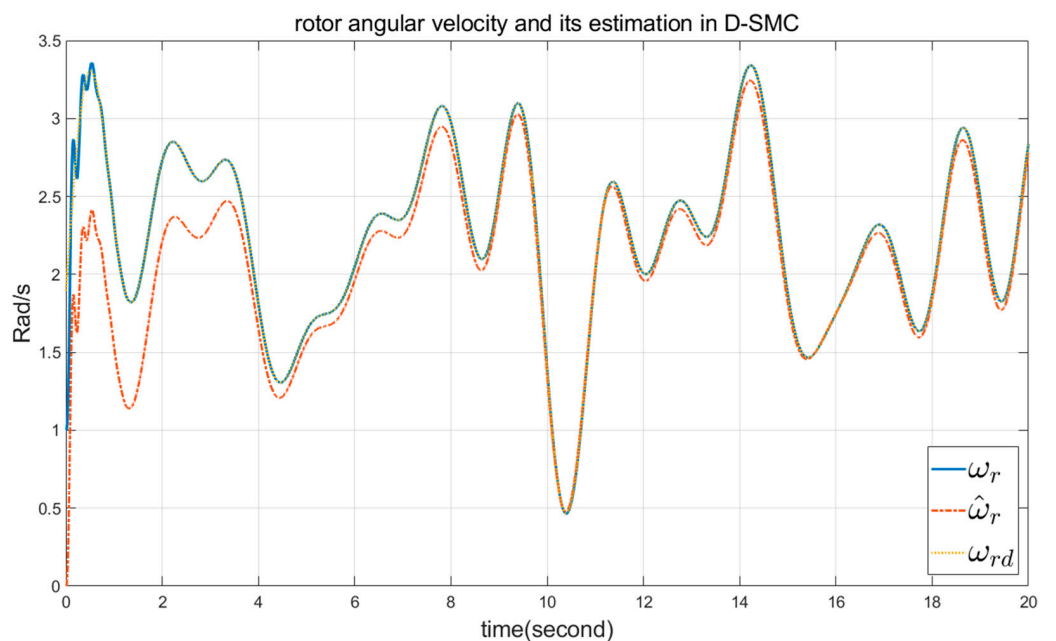
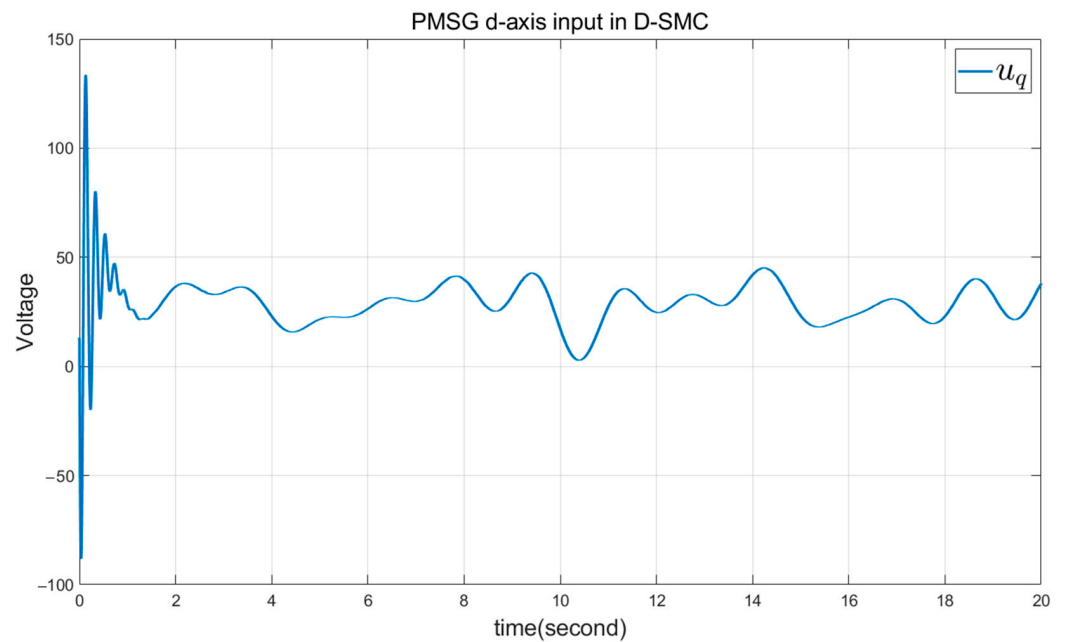
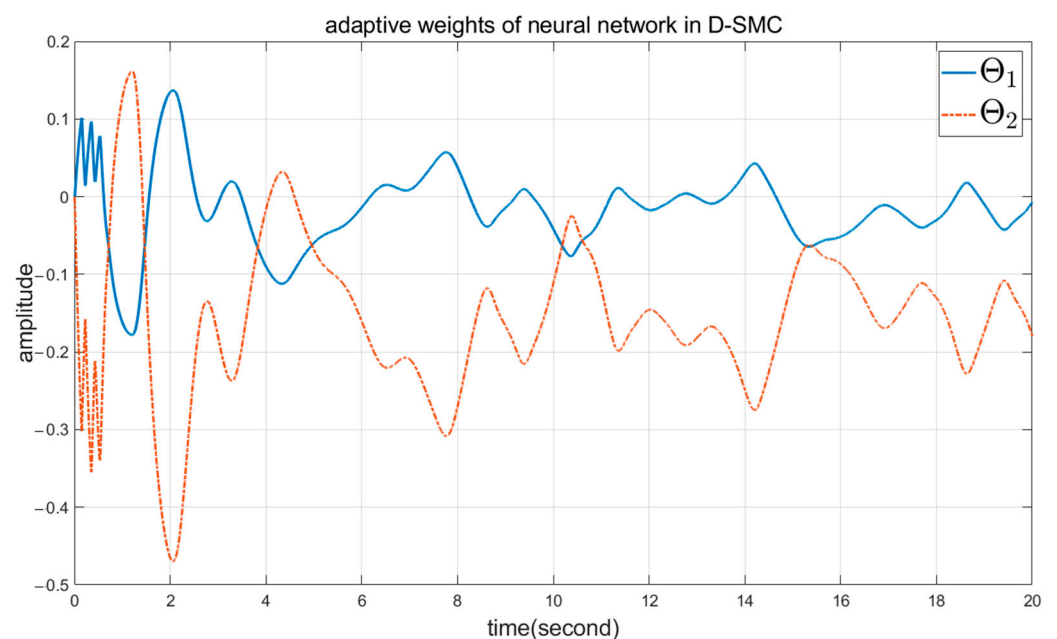


Figure 8. Performance of ONN in estimation and tracking using D-SMC.



**Figure 9.** Torque input of PMSG in q-axis using D-SMC.



**Figure 10.** Adaptive weights of ONN using D-SMC.

The advantage of the D-SMC approach is shown using the T-SMC with similar parameters. For example, the selected sliding coefficients in Equation (46) are  $c_1 = 10$  and  $c_2 = 0.1$ . Figures 11–14 show the simulation results. The sliding surface's finite-time convergence to zero can be seen, as in the previous example. Good tracking of the ONN state, rotor speed, and its desired signal can be seen. Figure 13 shows the available chattering in the torque signal, which cannot be applied to the actuator of the PMSG in the q-axis. The adaptive weights of the ONN are shown in Figure 14.

Based on Figures 7 and 11, one can see the sliding surface's convergence to zero happens in finite time in both approaches. From Figures 8 and 12, it is clear that when the wind speed is decreased (for example, at 10.4 s), the rotor angular velocity decreases to near zero due to the economic reasons. On the other hand, if the wind speed is increased (for example, at 14 s), the rotor angular velocity also increases. Figures 10 and 14 show

the adaptive weights of the neural network in both the D-SMC and T-SMC, respectively. Note that the initial oscillations in the D-SMC are due to the added integrator and are not chattering. High-frequency chattering can be seen in Figure 13, while Figure 9 indicates smoothness and is without chattering. Due to the available chattering in the d-axis input of the T-SMC, it cannot be applied to the PMSG.

These two simulations show the advantages of the T-SMC and D-SMC in the tracking of the desired signal and also the good performance of the proposed ONN. However, chattering is available in the T-SMC and can be suppressed in the D-SMC. This is what makes the D-SMC a priority over the T-SMC.

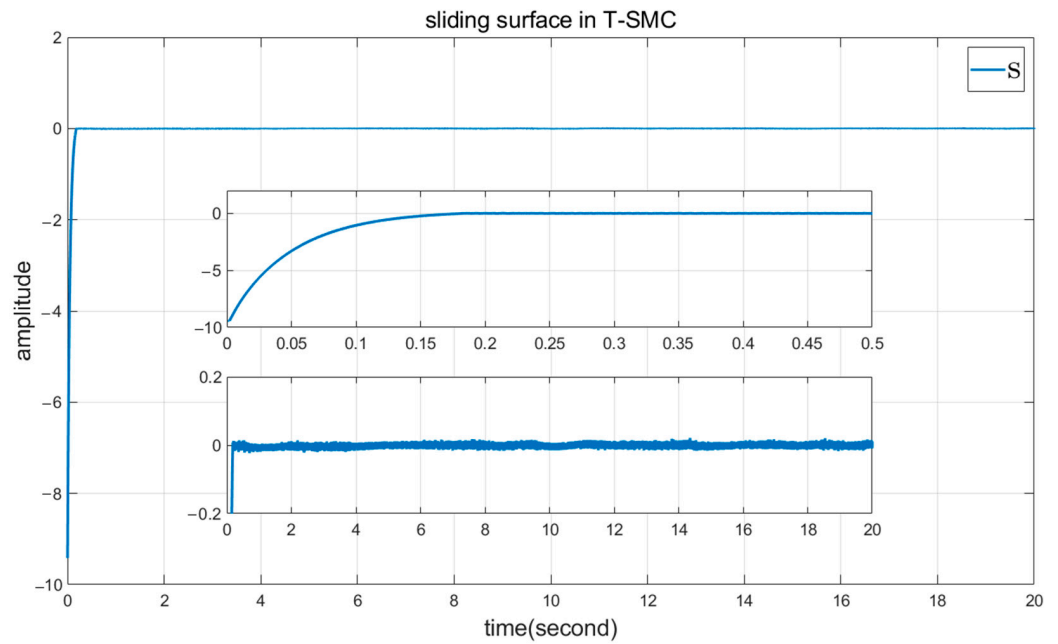


Figure 11. Finite-time sliding surface convergence to zero using T-SMC.

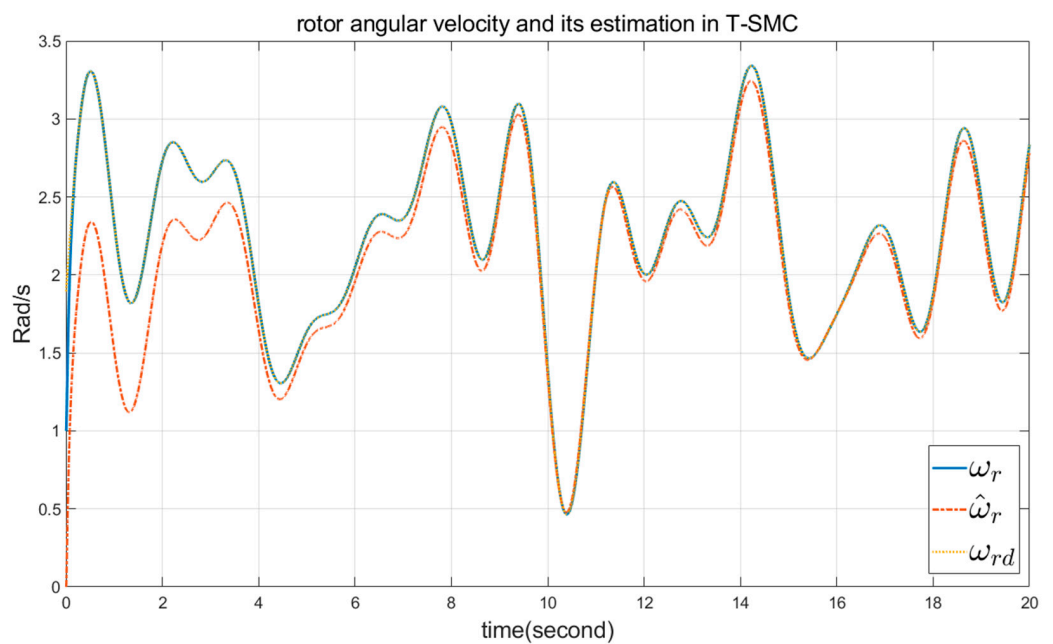


Figure 12. Performance of ONN in estimation and tracking using T-SMC.

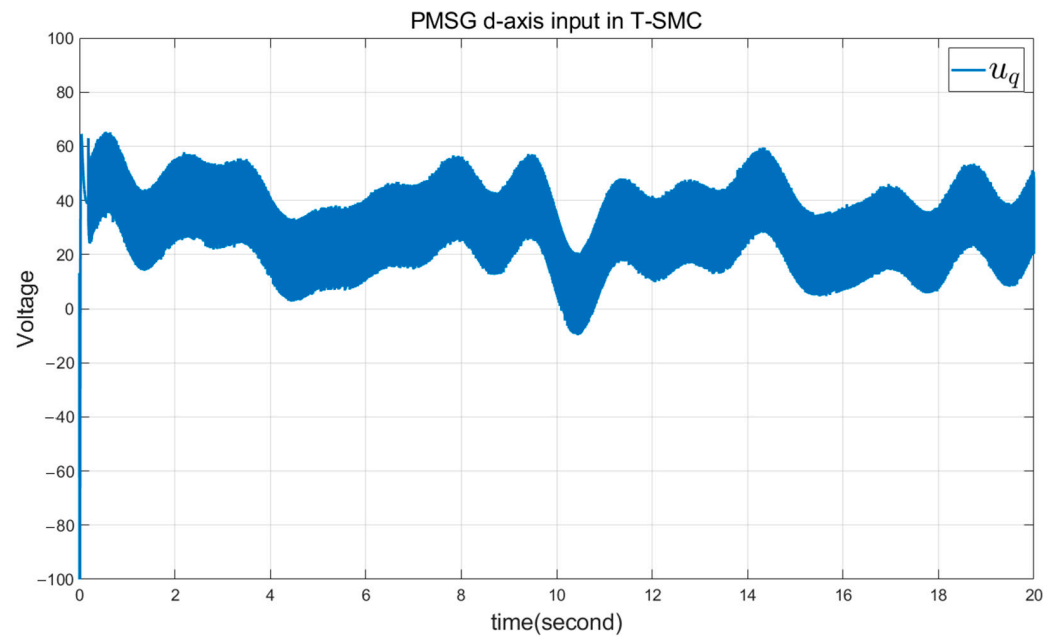


Figure 13. Torque input of PMSG in q-axis using T-SMC.

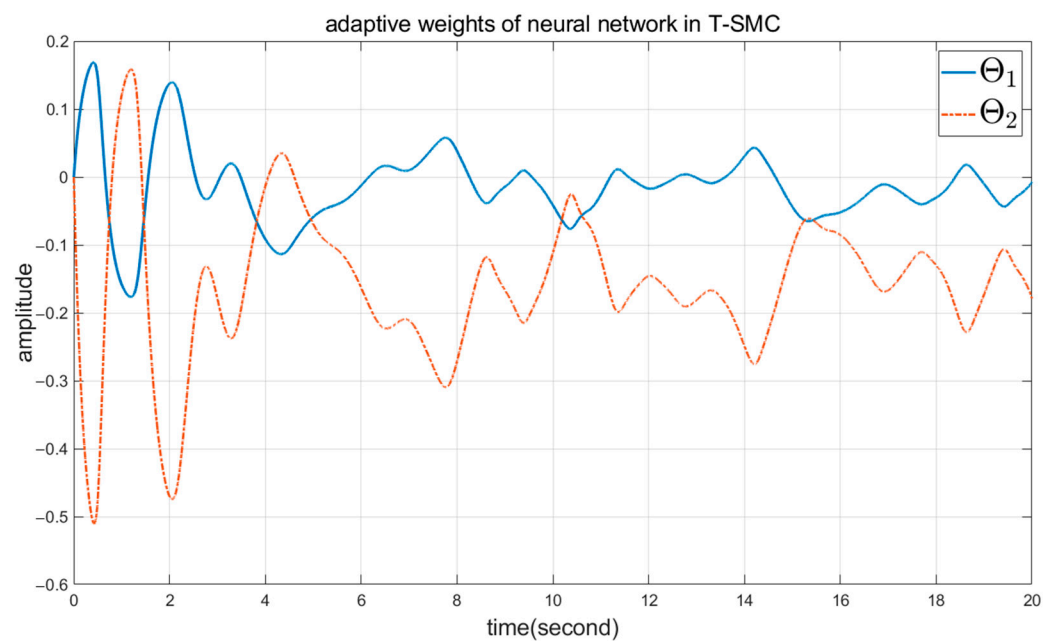


Figure 14. Adaptive weights of ONN using T-SMC.

### 6. Conclusions

A novel structure of torque control has been constructed for a VWT coupled to a PMSG. A PMSG has been described in d-q reference frameworks. In order to obtain a good performance, smooth control signals should be used as the inputs for the PMSG in both d-q directions. Moreover, the available uncertainties of the WT model are another issue which should be considered. To this end, a novel D-SMC is presented in this paper. Using the proposed D-SMC, high-frequency chattering is removed by a low-pass integrator filter. Then, to implement the D-SMC and to identify the extra state, an ONN is proposed. Moreover, the stability of the D-SMC and ONN has been proved using Lyapunov theory. Additionally, a comparison using the T-SMC has also been provided. To exhibit the fair advantages and superiority of the D-SMC over the T-SMC, a similar novel ONN was implemented in two SMC-based controllers. Chattering elimination results can be seen in

the D-SMC, while the chattering remains in the T-SMC. Moreover, the design procedure developed in this work shows the simplicity of the realization, and the concept for, the proposed D-SMC. Future works can be focused on the selection of other generators such as double-fed induction generators (DFIGs) and comparisons to the PMSG.

**Author Contributions:** A.K.-M.: analysis, writing—original draft and preparation; O.B.: conceptualization, reviewing, editing. All authors have read and agreed to the published version of the manuscript.

**Funding:** This study received no external funding.

**Data Availability Statement:** The original contributions presented in the study are included in the article, further inquiries can be directed to the corresponding author.

**Acknowledgments:** The authors wish to express their gratitude to the Basque Government, which provided support through the project EKOHEGAZ II (ELKARTEK KK-2023/00051); the Diputación Foral de Álava (DFA), which provided support through the project CONAVANTER; the UPV/EHU, which provided support through the project GIU23/002; and the MobilityLab Foundation (CONV23/14) for supporting this work.

**Conflicts of Interest:** The authors declare no conflicts of interest.

## References

- Burton, T.; Sharpe, D.; Jenkins, N.; Bossanyi, E. *Wind Energy Handbook*; Wiley: Hoboken, NJ, USA, 2001.
- Manwell, J.F.; McGowan, J.; Rogers, A. *Wind Energy Explained: Theory, Design and Applications*; Wiley: Hoboken, NJ, USA, 2002.
- Carlin, P.W.; Laxson, A.S.; Muljadi, E.B. The history and state of the art of variable-speed wind turbine technology. *Wind Energy Int. J. Prog. Appl. Wind. Power Convers. Technol.* **2003**, *6*, 129–159. [[CrossRef](#)]
- Song, Y.D.; Dhinakaran, B.; Bao, X.Y. Variable speed control of wind turbines using nonlinear and adaptive algorithms. *J. Wind Eng. Ind. Aerodyn.* **2000**, *85*, 293–308. [[CrossRef](#)]
- Su, H.; Dou, B.; Qu, T.; Zeng, P.; Lei, L. Experimental investigation of a novel vertical axis wind turbine with pitching and self-starting function. *Energy Convers. Manag.* **2020**, *217*, 113012. [[CrossRef](#)]
- Rahimi, M.; Parniani, M. Dynamic behavior and transient stability analysis of fixed speed wind turbines. *Renew. Energy* **2009**, *34*, 2613–2624. [[CrossRef](#)]
- Sumper, A.; Gomis-Bellmunt, O.; Sudri-Andreu, A.; Villafila-Robles, R.; Rull-Duran, J. Response of fixed speed wind turbines to system frequency disturbances. *IEEE Trans. Power Syst.* **2009**, *24*, 181–192. [[CrossRef](#)]
- Poultangari, I.; Shahnazi, R.; Sheikhan, M. RBF Neural network based PI pitch controller for a class of 5-MW wind turbines using particle swarm optimization algorithm. *ISA Trans.* **2012**, *51*, 641–648. [[CrossRef](#)]
- Barambones, O.; Cortajarena, J.A.; Calvo, I.; Gonzalez de Durana, J.M.; Alkorta, P.; Karami-Mollaei, A. Variable speed wind turbine control scheme using a robust wind torque estimation. *Renew. Energy* **2019**, *133*, 354–366. [[CrossRef](#)]
- Bianchi, F.D.; de Battista, H.; Mantz, R.J. *Wind Turbine Control Systems: Principles, Modelling and Gain Scheduling Design*; Springer Science and Business Media: London, UK, 2006.
- Camblong, H. Digital robust control of a variable speed pitch regulated wind turbine for above rated wind speeds. *Control Eng. Pract.* **2008**, *16*, 946–958. [[CrossRef](#)]
- Asgharniaa, A.; Shahnazi, R.; Jamali, A. Performance and robustness of optimal fractional fuzzy PID controllers for pitch control of a wind turbine using chaotic optimization algorithms. *ISA Trans.* **2018**, *79*, 27–44. [[CrossRef](#)] [[PubMed](#)]
- Oh, K.Y.; Park, J.Y.; Lee, J.S.; Lee, J. Implementation of a torque and a collective pitch controller in a wind turbine simulator to characterize the dynamics at three control regions. *Renew. Energy* **2015**, *79*, 150–160. [[CrossRef](#)]
- Abolvafaei, M.; Ganjefar, S. Maximum power extraction from a wind turbine using second-order fast terminal sliding mode control. *Renew. Energy* **2019**, *139*, 1437–1446. [[CrossRef](#)]
- Seker, M.; Zengeroglu, E.; Tatlicioglu, E. Non-linear control of variable-speed wind turbines with permanent magnet synchronous generators: A robust backstepping approach. *Int. J. Syst. Sci.* **2016**, *47*, 420–432. [[CrossRef](#)]
- Hand, M.M. *Variable-Speed Wind Turbine Controller Systematic Design Methodology: A Comparison of Nonlinear and Linear Model-Based Designs*; NREL report TP-500-25540; National Renewable Energy Laboratory: Golden, CO, USA, 1999.
- Ekelund, T. Speed control of wind turbines in the stall region. In Proceedings of the 1994 Proceedings of IEEE International Conference on Control and Applications (CCA), Glasgow, UK, 24–26 August 1994; pp. 227–232.
- Novak, P.; Ekelund, T.; Jovik, Y.; Schmidtbauer, B. Modeling and control of variable-speed wind-turbine drive system dynamics. *IEEE Control Syst. Mag.* **1995**, *15*, 28–38.
- Stol, K.A.; Fingersh, L.J. *Wind Turbine Field of State-Space Control Designs*; NREL/SR-500-35061; National Renewable Energy Laboratory: Golden, CO, USA, 2004.



20. Bossoufi, B.; Karim, M.; Lagrioui, A.; Taoussi, M.; Derouich, A. Observer backstepping control of DFIG-generators for wind turbines variable-speed: FPGA based implementation. *Renew. Energy* **2015**, *81*, 903–917. [[CrossRef](#)]
21. Elsis, M. New design of adaptive model predictive control for energy conversion system with wind torque effect. *J. Clean. Prod.* **2019**, *240*, 118265. [[CrossRef](#)]
22. Abolvafaei, M.; Ganjefar, S. Adaptive second-order terminal PID sliding mode control design for integer-order approximation of wind turbine system for maximum power extraction. *IET Control Theory Appl.* **2021**, *15*, 2210–2220. [[CrossRef](#)]
23. Subramaniyam, R.; Joo, Y.H. Memory-based ISMC design of DFIG-based wind turbine model via T-S fuzzy approach. *IET Control Theory Appl.* **2021**, *15*, 348–359. [[CrossRef](#)]
24. Slotine, J.J.E.; Li, W. *Applied Nonlinear Control*; Prentice Hall: Englewood Cliffs, NJ, USA, 1991.
25. Perruquetti, W.; Barbot, J.P. *Sliding Mode Control in Engineering*; CRC Press: Boca Raton, FL, USA, 2002. [[CrossRef](#)]
26. Karami-Mollae, A.; Pariz, N.; Shانهchi, H.M. Position control of servomotors using neural dynamic sliding mode. *J. Dyn. Syst. Meas. Control* **2011**, *133*, 141–150. [[CrossRef](#)]
27. Karami-Mollae, A.; Tirandaz, H.; Barambones, O. Dynamic sliding mode position control of induction motors based load torque compensation using adaptive state observer. *COMPEL-Int. J. Comput. Math. Electr. Electron. Eng.* **2018**, *37*, 2249–2262. [[CrossRef](#)]
28. Suleimenov, K.; Sarsembayev, B.; Hong Phuc, B.D.; Do, T.D. Disturbance observer-based integral sliding mode control for wind energy conversion systems. *Wind Energy* **2020**, *23*, 1026–1047. [[CrossRef](#)]
29. Alsaadi, F.E.; Yasami, A.; Alsubaie, H.; Alotaibi, A.; Jahanshahi, H. Control of a hydraulic generator regulating system using Chebyshev-neural-network-based non-singular fast terminal sliding mode method. *Mathematics* **2023**, *11*, 168. [[CrossRef](#)]
30. Lee, H.; Utkin, V.I. Chattering suppression methods in sliding mode control systems. *Annu. Rev. Control* **2007**, *31*, 179–188. [[CrossRef](#)]
31. Fuh, C.-C. Variable-thickness boundary layers for sliding mode control. *J. Mar. Sci. Technol.* **2008**, *16*, 288–294. [[CrossRef](#)]
32. Chen, H.-M.; Renn, J.-C.; Su, J.-P. Sliding mode control with varying boundary layers for an electro-hydraulic position servo system. *Int. J. Adv. Manuf. Technol.* **2005**, *26*, 117–123. [[CrossRef](#)]
33. Zhang, X. Sliding mode-like fuzzy logic control with adaptive boundary layer for multiple-variable discrete. *J. Intell. Syst.* **2016**, *25*, 209–220. [[CrossRef](#)]
34. Gandikota, G.; Das, D.K. Disturbance observer-based adaptive boundary layer sliding mode controller for a type of nonlinear multiple-input multiple-output system. *Int. J. Robust Nonlinear Control* **2019**, *29*, 5886–5912. [[CrossRef](#)]
35. Cucuzzella, M.; Incremona, G.P.; Ferrara, A. Design of robust higher order sliding mode control for microgrids. *IEEE J. Emerg. Sel. Top. Circuits Syst.* **2015**, *5*, 393–401. [[CrossRef](#)]
36. Nonaka, R.; Yamashita, Y.; Tsubakino, D. General scheme for design of higher-order sliding-mode controller. In Proceedings of the American Control Conference (ACC), Chicago, IL, USA, 1–3 July 2015; pp. 5176–5181.
37. Levant, A. Sliding order and sliding accuracy in sliding mode control. *Int. J. Control* **1993**, *58*, 1247–1263. [[CrossRef](#)]
38. Levant, A. Homogeneity approach to high-order sliding mode design. *Automatica* **2005**, *41*, 823–830. [[CrossRef](#)]
39. Plestan, F.; Glumineau, A.; Laghrouche, S. A new algorithm for high-order sliding mode control. *Int. J. Robust Nonlinear Control* **2008**, *18*, 441–453. [[CrossRef](#)]
40. Levant, A. Higher-order sliding modes, differentiation and output-feedback control. *Int. J. Robust Nonlinear Control* **2010**, *76*, 924–941. [[CrossRef](#)]
41. Yang, Y.; Qin, S.; Jiang, P. A modified super-twisting sliding mode control with inner feedback and adaptive gain schedule. *Int. J. Adapt. Control Signal Process.* **2017**, *31*, 398–416. [[CrossRef](#)]
42. Butt, Q.R.; Bhatti, A.I.; Mufti, M.R.; Rizvi, M.A.; Awan, I. Modeling and online parameter estimation of intake manifold in gasoline engines using sliding mode observer. *Simul. Model. Pract. Theory* **2013**, *32*, 138–154. [[CrossRef](#)]
43. Davila, J.; Fridman, L.; Levant, A. Second-order sliding mode observer for mechanical systems. *IEEE Trans. Autom. Control* **2005**, *50*, 1785–1789. [[CrossRef](#)]
44. Hwang, S.; Park, J.B.; Joo, Y.H. Disturbance observer-based integral fuzzy sliding-mode control and its application to wind turbine system. *IET Control Theory Appl.* **2019**, *13*, 1891–1900. [[CrossRef](#)]
45. Liu, L.; Fei, J.; Yang, X. Adaptive interval type-2 fuzzy neural network sliding mode control of nonlinear systems using improved extended state observer. *Mathematics* **2023**, *11*, 605. [[CrossRef](#)]
46. Karami-Mollae, A.; Barambones, O. Sliding observer in sliding mode control of multi-inputs fractional order chaotic systems. *Pramana-J. Phys.* **2022**, *96*, 180–197. [[CrossRef](#)]
47. Liu, Y.-T.; Kung, T.-T.; Chang, K.-M.; Chen, S.-Y. Observer-based adaptive sliding mode control for pneumatic servo system. *Precis. Eng.* **2013**, *37*, 522–530. [[CrossRef](#)]
48. Xia, Y.; Zhu, Z.; Fu, M. Back-stepping sliding mode control for missile systems based on an extended state observer. *IET Control Theory Appl.* **2011**, *5*, 93–102. [[CrossRef](#)]
49. Xiong, Y.; Saif, M. Sliding mode observer for nonlinear uncertain systems. *IEEE Trans. Autom. Control* **2001**, *46*, 2012–2017. [[CrossRef](#)]
50. Mseddi, A.; Naifar, O.; Rhaima, M.; Mchiri, L.; Ben Makhlouf, A. Robust control for torque minimization in wind hybrid generators: An H-Infinity approach. *Mathematics* **2023**, *11*, 3557. [[CrossRef](#)]
51. Benchaib, A.; Rachid, A.; Audrezet, E.; Tadjine, M. Real-time sliding-mode observer and control of an induction motor. *IEEE Trans. Ind. Electron.* **1999**, *46*, 128–138. [[CrossRef](#)]

52. Boukhezzar, B.; Siguerdidjane, H. Nonlinear control of a variable-speed wind turbine using a two-mass model. *IEEE Trans. Energy Convers.* **2010**, *26*, 149–162. [[CrossRef](#)]
53. Lin, Z.; Liu, J.; Niu, Y. Dynamic response regulation of non-linear feedback linearised wind turbine using a two-mass. *IET Control Theory Appl.* **2017**, *11*, 816–826. [[CrossRef](#)]
54. Zhang, C.; Plestan, F. Adaptive sliding mode control of floating offshore wind turbine equipped by permanent magnet synchronous generator. *Wind Energy* **2021**, *24*, 754–769. [[CrossRef](#)]
55. Li, T.; Tao, L.; Xu, B. Linear parameter varying observer-based adaptive dynamic surface sliding mode control for PMSM. *Mathematics* **2024**, *12*, 1219. [[CrossRef](#)]
56. Bossanyi, E.A.; Wright, A.D.; Fleming, P.A. *Controller Field Tests on the NREL CART2 Turbine*; No. NREL/TP-5000-49085; National Renewable Energy Lab (NREL): Golden, CO, USA, 2010.

**Disclaimer/Publisher’s Note:** The statements, opinions and data contained in all publications are solely those of the individual author(s) and contributor(s) and not of MDPI and/or the editor(s). MDPI and/or the editor(s) disclaim responsibility for any injury to people or property resulting from any ideas, methods, instructions or products referred to in the content.